JGR Space Physics

RESEARCH ARTICLE
10.1029/2020JA028557

A Case Study of Nonresonant Mode 3-s ULF Waves Observed by MMS

Shan Wang[1,2], Li-Jen Chen[2], Jonathan Ng[1,2], Naoki Bessho[1,2], Guan Le[2], Shing F. Fung[2], Daniel J. Gershman[2], and Barbara L. Giles[2]

[1]Astronomy Department, University of Maryland, College Park, MD, USA, [2]NASA Goddard Space Flight Center, Greenbelt, MD, USA

Key Points:
- A 3-s ULF wave event observed by MMS in a foreshock region is determined to be due to the nonresonant ion beam instability
- Solar wind ions lose energies to the transverse wave field and are decelerated along the background magnetic field by the Lorentz force
- The ULF wave leads to electron heating and excites secondary waves

Correspondence to:
S. Wang,
swang90@umd.edu

Citation:
Wang, S., Chen, L.-J., Ng, J., Bessho, N., Le, G., Fung, S. F., et al. (2020). A case study of nonresonant mode 3-s ULF waves observed by MMS. *Journal of Geophysical Research: Space Physics*, *125*, e2020JA028557. https://doi.org/10.1029/2020JA028557

Received 4 AUG 2020
Accepted 3 NOV 2020
Accepted article online 16 NOV 2020

Abstract The nature of the 3-s ultralow frequency (ULF) wave in the Earth's foreshock region and the associated wave-particle interaction are not yet well understood. We investigate the 3-s ULF waves using Magnetospheric Multiscale (MMS) observations. By combining the plasma rest frame wave properties obtained from multiple methods with the instability analysis based on the velocity distribution in the linear wave stage, the ULF wave is determined to be due to the ion/ion nonresonant mode instability. The interaction between the wave and ions is analyzed using the phase relationship between the transverse wave fields and ion velocities and using the longitudinal momentum equation. During the stage when ULF waves have sinusoidal waveforms up to $|dB|/|B_0| \sim 3$, where dB is the wave magnetic field and B_0 is the background magnetic field, the wave electric fields perpendicular to $\boldsymbol{B}_0$ do negative work to solar wind ions; along $\boldsymbol{B}_0$, a longitudinal electric field develops, but the $V \times B$ force is stronger and leads to solar wind ion deceleration. During the same wave stage, the backstreaming beam ions gain energy from the transverse wave fields and get deceleration along $\boldsymbol{B}_0$ by the longitudinal electric field. The ULF wave leads to electron heating, preferentially in the direction perpendicular to the local magnetic field. Secondary waves are generated within the ULF waveforms, including whistler waves near half of the electron cyclotron frequency, high-frequency electrostatic waves, and magnetosonic whistler waves. The work improves the understanding of the nature of 3-s ULF waves and the associated wave-particle interaction.

1. Introduction

The foreshock region is upstream of the Earth's bow shock with magnetic connectivity to the shock and filled with backstreaming particles from the shock (e.g., Eastwood et al., 2005). The interaction of multiple plasma populations in the foreshock generates a variety of waves. The ultralow frequency (ULF) wave in the foreshock typically has the spacecraft frame frequency below 1 Hz, which is understood to be mainly associated with the interaction between the incoming solar wind ions and backstreaming ions (e.g., review by Wilson, 2016). The foreshock ULF wave power could be transmitted into the magnetosphere (e.g., Engebretson et al., 1991; Yeoman et al., 2012) or excite additional ULF waves in the magnetosphere (e.g., Chi et al., 1994; Wang et al., 2019). Open questions still remain about the nature of the foreshock ULF waves and the wave-particle interaction. The properties of the waves are better resolved with high time resolution of fields and particle measurements by the Magnetospheric Multiscale (MMS) mission, which motivate us to look into the ULF wave observations by MMS.

The electromagnetic ion beam instability consists of a few types. The field-aligned counterstreaming beams with a relative drift (V_d) of at least the ion Alfven speed (V_A) can excite the right-handed resonant mode, left-handed resonant mode, and right-handed nonresonant mode (Gary, 1991). The polarization is with respect to the background magnetic field in the plasma rest frame. The ion cyclotron resonant condition is satisfied when the cyclotron resonant velocity ($\boldsymbol{V_{res}}$) is within the thermal speed (V_{th}) from the bulk velocity ($\boldsymbol{V_0}$) of an ion population ($|\boldsymbol{V_{res}}\text{-}\boldsymbol{V_0}| < V_{th}$), so that a large number of particles could be in resonance, where

$$\omega - \boldsymbol{k} \cdot \boldsymbol{V_{res}} = n\omega_{ci},\ n = \pm 1 \tag{1}$$

ω_{ci} is the ion cyclotron frequency, $V_{th} = \sqrt{2k_BT/m}$, and k_B is the Boltzmann constant. The "resonant mode" instability refers to the wave that resonates with the beam (backstreaming) ions with $n = \pm 1$, and

the resulting wave propagates along the same direction with the beam in the plasma rest frame. The "nonresonant" mode means that the wave is not in resonance with the beam ions; the wave may not be resonant with the solar wind ions either, while the parallel anisotropy due to the large effective parallel pressure of the counterstreaming ions excites the firehose-like nonresonant instability (e.g., Winske & Leroy, 1984). However, in certain regimes the wave could be in resonance with the solar wind ions (Akimoto et al., 1993; Weidl et al., 2019). The wave resulting from the nonresonant instability propagates toward the solar wind ions. Overall, a low density ratio between the beam (n_{beam}) and plasmas (n_0) ($n_{beam}/n_0 < 0.05$) favors the right-hand resonant mode ($n = -1$ resonance with the beam), while increasing n_{beam}/n_0 and V_d **(>> V_A)** leads to dominance of the nonresonant mode (Akimoto et al., 1993; Wilson, 2016). When the beam population is hot ($V_{th,\mathrm{beam}} > V_{0,\mathrm{beam}}$), many beam ions move opposite to the bulk velocity of the beam population, and the ($n = 1$) cyclotron resonance with such a population generates the left-hand resonant mode (e.g., Gary, 1991). For all three modes, the maximum growth rate typically occurs at the field-aligned propagation direction, the plasma rest frame frequency is smaller than ω_{ci}, and the wavelength is much larger than the ion inertial length (d_i).

Considerable efforts have been made to understand the ULF waves in the foreshock region. Quasi-monochromatic ULF waves mainly have three types based on their characteristic periods in the spacecraft frame: 30-s waves, 10-s waves, and the 3-s waves. The 30-s wave is consistent with the right-handed resonant mode being the fast mode wave, based on the plasma rest frame (approximated to be the solar wind frame) phase velocity that has a sunward component and right-handed polarization (e.g., Eastwood et al., 2005). The Cluster mission with 4-s resolution particle measurements enabled analyses of particle distributions in 30-s ULF waves, revealing the pitch angle scattering of beam ions by the wave (e.g., Mazelle et al., 2003). The 10-s wave properties are consistent with the left-handed resonant mode that generates Alfvenic waves, based on the plasma rest frame sunward propagation and left-handed polarization, and the wave is associated with hot diffuse ion distributions as expected for left-handed mode wave (e.g., Eastwood et al., 2003). The 3-s wave is least understood, because the wave phase velocity is usually close to the plasma velocity (Hobara et al., 2007; Le et al., 1992), leaving significant uncertainties in determining the plasma rest frame propagation and polarization. The waves have the period of 1–10 s and right-handed polarization in the spacecraft frame. If the wave propagates with a sunward component in the plasma rest frame, the intrinsic polarization would be left handed, consistent with the left-handed resonant mode, as suggested by a statistical analysis of the plasma rest frame wave properties (Hobara et al., 2007). If the wave propagates antisunward in the plasma rest frame, the intrinsic polarization would be right handed, consistent with the nonresonant mode. The nonresonant mode for 3-s waves was suggested in a case study using the estimated rest frame wave propagation (Li et al., 2013) and in another case study using the linear instability analysis based on typical plasma conditions in the foreshock (Blanco-Cano et al., 1999).

In this study, we analyze an event of 3-s ULF waves observed by the MMS mission, at the marginally quasi-parallel portion of the Earth's foreshock. The plasma rest frame wave properties are determined using multiple methods. We also perform the linear instability analysis based on the observed plasma distributions in the linear wave stage. The wave is concluded to be due to the right-handed nonresonant ion beam instability. With high-resolution plasma and field measurements, we discuss the interaction between the wave and ions, electron heating, and additional secondary waves in the 3-s ULF wave.

2. Data

Measurements from MMS are utilized. The Direct Current (DC)-coupled magnetic fields are from the FluxGate Magnetometer (FGM) at 128 samples/s (Russell et al., 2016), and the Alternating Current (AC)-coupled magnetic fields are from the Search Coil Magnetometer (SCM) at 8,192 samples/s (Le Contel et al., 2016). The wave power spectrogram in Figure 6b uses the merged data between FGM and SCM (Argall et al., 2018). Electric fields are from the axial (Ergun et al., 2016) and spin-plane double probes (Lindqvist et al., 2016), at 32 samples/s and 8,192 samples/s. Plasma data are from the Fast Plasma Investigation (FPI), with 150-ms resolution for ions and 30-ms resolution for electrons (Pollock et al., 2016).

Unless otherwise noted, the wave is discussed in the field-aligned coordinate relative to the background magnetic field $\boldsymbol{B}_0$ = 3.5×[−0.871, 0.489, 0.050] GSE, the average magnetic field during 04:53:50–04:54:00 UT (Figure 1b). The corresponding cone angle between B_0 and X_{GSE} is 30°. Taking the average magnetic field

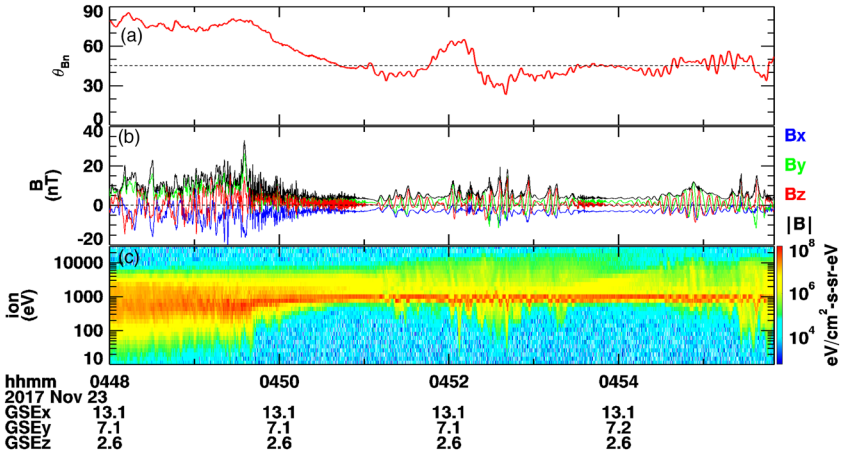

Figure 1. Overview of the foreshock region. (a) The angle between the local 30-s smoothed MMS1 magnetic field and the shock normal direction based on the bow shock model. Around 04:54 UT, the spacecraft is upstream of the shock with quiet fields, and the angle represents the shock normal angle that is slightly below 45°. (b) ULF wave magnetic fields in the GSE coordinate. (c) Ion spectrogram.

during a longer interval up to 40 s only makes a difference of 1° for the $\boldsymbol{B}_0$ direction. According to the magnetic fields measured by ARTEMIS-B at $X_{\mathrm{GSE}} \sim 38\ R_E$, the cone angle decreases from 48° to 30° during 04:40–05:00 UT, and the variation of the cone angle during each 2-min interval is up to ~8°. Our analysis focuses on the ULF waves observed within 2 min, and hence, the uncertainty in the $\boldsymbol{B_0}$ direction is estimated to be up to 8°. The x direction of the field-aligned coordinate is along $-\boldsymbol{B_0}$, such that the incoming solar wind ions mainly move with $v_x < 0$ and backstreaming beam ions move with $v_x > 0$. $\widehat{y} = (B_0 \times X_{GSE}) \times B_0$ and $\widehat{z} = -B_0 \times X_{GSE}$ are perpendicular to $\boldsymbol{B_0}$ and x-y-z form a right-handed coordinate.

3. Observation Results

MMS observed a foreshock region with ULF waves on 23 November 2017 (Figure 1). The spacecraft crossed the bow shock from downstream to upstream at about 04:50 UT, as the ion spectrogram becomes narrower (Figure 1c) and the magnetic field strength becomes weaker (Figure 1b). Figure 1a shows the angle between the local magnetic field and the bow shock normal, where the shock normal direction is based on the bow shock model (Farris et al., 1991), and the magnetic field uses the 30-s smoothed fields from MMS1 measurements. When the magnetic field is relatively quiet and could represent that upstream of the shock (B_0), such as around 04:53:50–04:54:00, the angle represents the shock normal angle (θ_{Bn}). The θ_{Bn} is close to and slightly below 45°, indicating the shock geometry to be marginally quasi-parallel, supported by the rich energetic particles beyond the solar wind energy range backstreaming from the shock (Figures 1c and 5h). The wave fluctuations are on and off repeatedly, which may suggest that the location is close to the boundary of the region with ULF waves.

3.1. ULF Wave Properties

The variation of the ULF wave during 04:53:50–04:55:50 UT is interpreted as the development of the wave (Figure 2). The wave is first observed with $|dB|/|B_0| \sim 0.2$ at 04:53:50–04:54:20 UT (will be referred to as the quasi-linear stage below) and grows to $|dB|/|B_0| > 1$ up to 3 during 04:54:30–04:55:15 UT, while the waveform remains close to be sinusoidal (Figure 2b). During 04:55:15–04:55:50 UT, the waveform steepens, deviating from the sinusoidal waveform, and $|dB|/|B_0|$ reaches 4. Since the observed wave frequency remains the same, we adopt a simple interpretation that the wave amplitude variation is due to the wave growth, although the spatial inhomogeneity may cause the spacecraft to transition between regions with different wave amplitudes. Figures 2e–2f show the wavelet power spectra of the magnetic fields for the right-handed and left-handed components (in the spacecraft frame), respectively. The total magnetic field data are rotated to the field-aligned coordinate relative to B_0 defined in section 2. After obtaining the wavelet transformation (complex numbers) for the two perpendicular components of the magnetic

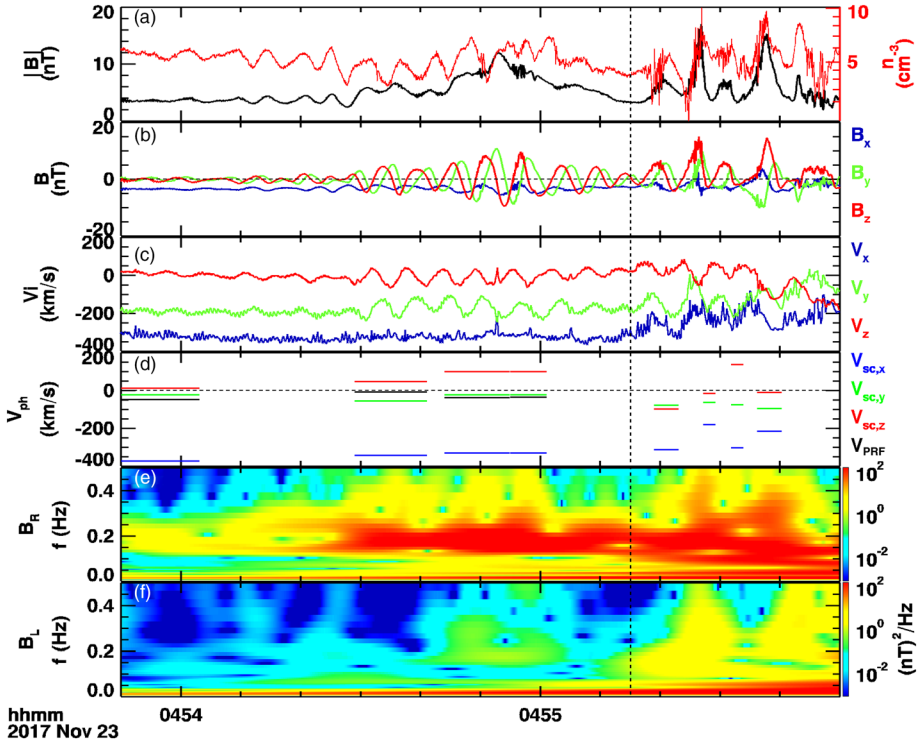

Figure 2. ULF wave properties. (a) Magnetic field strength (black) and electron number density (red). (b) Magnetic fields in the field-aligned coordinate defined in section 2. The wave starts to be observed at 04:53:50–04:54:20 UT with $|dB|/|B_0| \sim 0.2$, develops into larger-amplitude sinusoidal fluctuations up to $|dB|/|B_0| = 3$ during 04:54:20–04:55:15 UT. The fluctuations at 04:55:15–04:55:50 UT exhibit irregular waveforms. (c) Ion bulk velocity. (d) Wave phase velocities deduced from the correlation analysis of four-spacecraft magnetic fields using data in each segment. The blue-green-red curves are for the three components in the field-aligned coordinate in the spacecraft frame. The black curve is the phase velocity in the plasma rest frame, where positive values indicate a propagation toward the Sun. (e, f) Wavelet power spectra of the magnetic fields split into right-hand and left-hand components in the spacecraft frame.

field $B_{\perp 1}$ and $B_{\perp 2}$ ($\perp 1 = \hat{y}$, $\perp 2 = -\hat{z}$, such that ($\perp 1$, $\perp 2$, B_0) form a right-handed coordinate), the right-handed component is constructed as $B_R = B_{\perp 1} + iB_{\perp 2}$, and the left-handed component is $B_L = B_{\perp 1} - iB_{\perp 2}$. The power spectra show that the wave power is mainly at 0.1–0.3 Hz peaked at 0.16 Hz in the spacecraft frame, dominant in the right-hand component. The wave period is ~6 s, belonging to the so-called "3-s ULF wave" (Le et al., 1992).

The wave propagation property is determined using multiple methods. First, we perform the correlation analysis of the magnetic field using measurements from four spacecraft, where the average spacecraft separation is 22 km. The band-pass fields at 0.1–0.3 Hz are used. A time delay is obtained from the correlation analysis for each of MMS2, MMS3, and MMS4 with MMS1. Together with the positions of the four spacecraft, the amplitude and direction of the wave propagation could be obtained from the four-spacecraft timing method (Schwartz, 1998). In Figure 2d, the blue-green-red curves represent the resulting phase speed (V_{ph}) in the spacecraft frame, using data in the interval of each segment; the black lines (for sinusoidal wave intervals) mark the plasma rest frame phase velocity, where the plasma rest frame is determined by the ion bulk velocity (Figure 2c), where positive values mean sunward propagation, and the average ion bulk velocity during the corresponding interval is used as the plasma frame velocity. In the quasi-linear wave interval (04:53:50–04:54:03 UT), the spacecraft frame V_{ph} is 374×[−0.895, 0.427, 0.126] GSE km/s, 4° from $\boldsymbol{B_0}$. With the frequency of 0.16 Hz at the maximum wave power, the corresponding wavelength is $|V_{ph}|/f$ = 2,338 km, and kd_i = 0.26, where d_i = 97 km is the ion inertial length based on the background density of n_0 = 5.5 cm^{-3}. In the plasma rest frame, f = 0.020 Hz = 0.38 f_{ci}, V_{ph} = 47 km/s = 1.4 V_A toward the Earth, where f_{ci} = 0.053 Hz is based on B_0, and V_A = 33 km/s is the ion Alfven speed based on the background B_0 and n_0. Applying the minimum variance analysis of

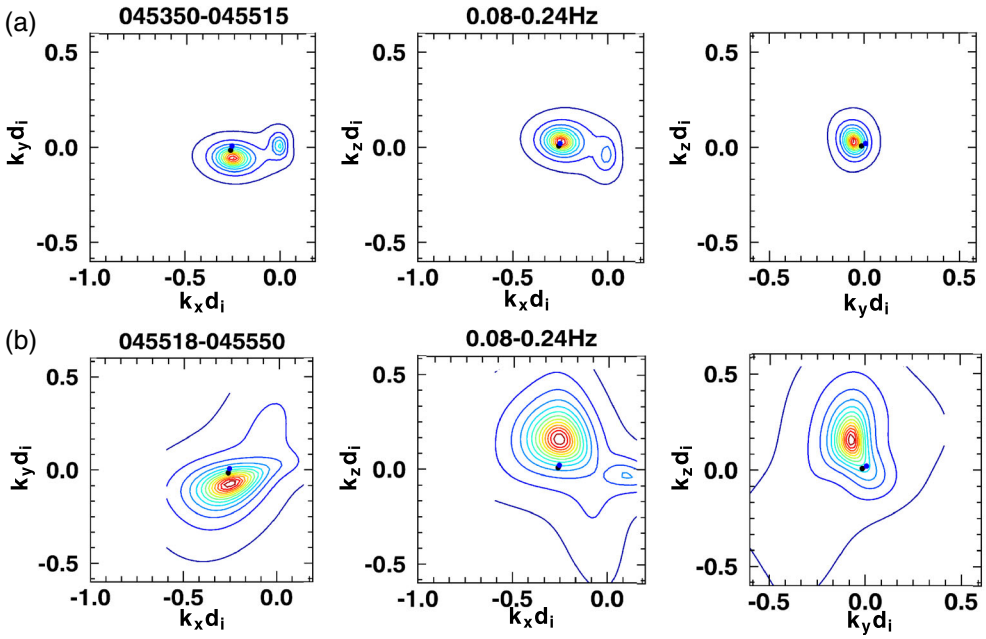

Figure 3. Wavenumber determined from the k-filter technique. (a, b) The two rows show the magnetic wave power as contours in three planes for the interval before and after the dashed vertical line in Figure 2, cut through the wavenumber with the maximum wave power. The black and blue dots mark the results from the magnetic field correlation analysis and the $\boldsymbol{J} \times \boldsymbol{B}$ method, respectively.

the magnetic field, we obtain the propagation direction from the minimum variance direction as [−0.950, 0.312, −0.017] GSE, consistent with the above-mentioned correlation analysis result within 11°. Figure 2d shows that the obtained V_{ph} at different times are roughly consistent before the nonlinear stage. The spacecraft frame V_{ph} for the sinusoidal wave interval varies at 338–374 km/s, and the range of 36 km/s is considered as the uncertainty of the V_{ph} calculation. In the irregular waveform interval, the amplitude of the x component of V_{ph} in the spacecraft frame decreases as the wave amplitude grows.

Second, we apply the k-filter technique to obtain the wavenumber (Pinc¸on & Motschmann, 1998), which was demonstrated to be a valid method applying to Alfvenic turbulence using MMS measurements (Gershman et al., 2018). The cross spectral density matrix is constructed as a function of ω and k using magnetic fields and relative positions of the four spacecraft. The basic assumption is that the wave field is a superposition of propagating waves propagating described as $exp^{i(\boldsymbol{k} \cdot \boldsymbol{r} - \omega t)}$, and after the matrix manipulation, the wave power at each ω and k is "filtered" out. The method is applied to two intervals: sinusoidal ULF wave 04:53:50–04:55:15 UT and irregular waveform 04:55:18–04:55:50 UT. For each interval, sliding window-averaged Fast Fourier Transformation (FFT) of the magnetic fields with a set of 800 points with Hanning window applied is used to construct the k-filtering power spectra. The $\nabla \cdot \boldsymbol{B} = 0$ constraint is applied in the k-filtering algorithm. Figure 3 shows the contours of the power spectra (warm colors represent higher power) in three k planes, cut through the wavenumber with maximum power, where each row is for the results of an interval, and hence, the k at the center of the red contours are those determined by the k-filter method. The corresponding spacecraft frame frequency range is labeled on top of the middle panel. In each panel, the black dots mark the wavenumber determined from the first method of correlation analysis, by using the average spacecraft frame V_{ph} shown in Figure 2c that lie in the same interval with the k-filtering analysis and the spacecraft frame frequency of 0.16 Hz. The blue dots mark the results from a third method based on Ampere's law $\boldsymbol{k}(\omega) = i\mu_0 \boldsymbol{J}(\omega) \times \boldsymbol{B}(\omega)/|\boldsymbol{B}(\omega)|^2$ (Bellan, 2016) that is applied to the same k-filtering analysis interval, where $\boldsymbol{J}(\boldsymbol{\omega})$ is the FFT of the current density deduced from the curlometer technique [Robert et al., 1998] and $\boldsymbol{B}(\omega)$ is the FFT of the averaged magnetic field over four spacecraft. The results show good consistency between the three methods, although the k-filter technique tends to give a slightly larger $k_\perp$ compared to the other two.

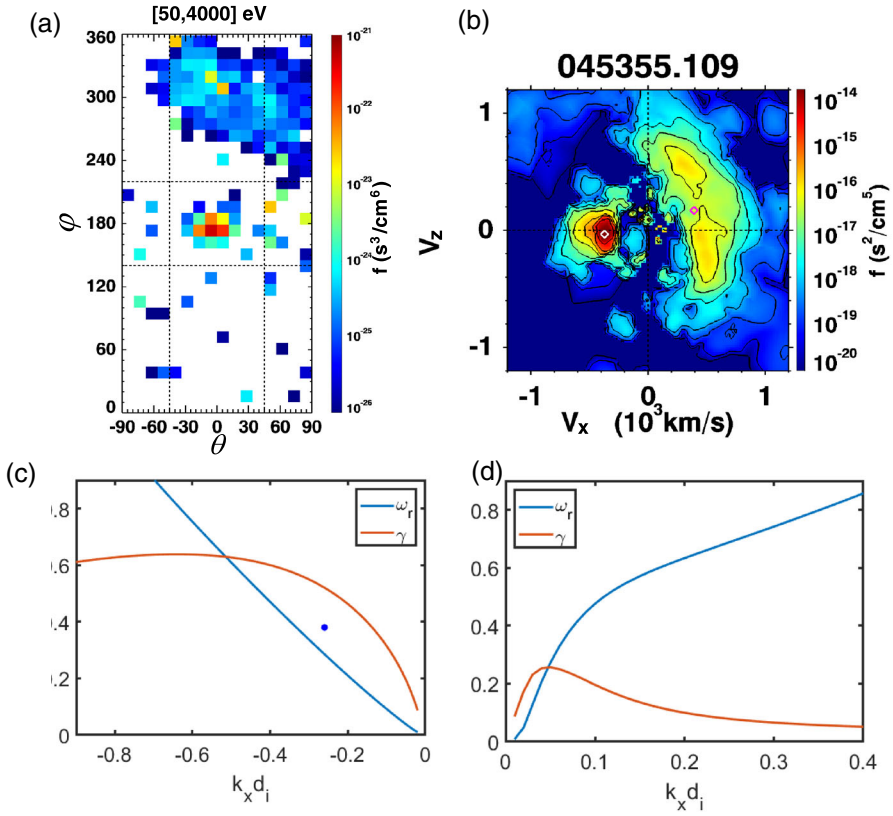

Figure 4. The linear instability analysis. (a) The averaged ion phase space density over 50–4,000 eV as a function of the instrument polar (θ) and azimuthal angles (φ), in the linear wave interval. (b) The reduced ion distribution at the same time with (a) in the $v_x - v_z$ plane of the field-aligned coordinate. The white and magenta diamonds mark the bulk velocities of the solar wind and the reflected beam, respectively. (c, d) The dispersion relation based on the plasma condition in the linear wave interval for the nonresonant (c) and resonant (d) modes, where ω_r and γ are the real and imaginary parts of the frequency. The blue dot in (c) marks the real frequency and the wavenumber for MMS observations.

Based on the above estimated wave properties in the quasi-linear wave interval, the wave propagates anti-sunward in the plasma rest frame, same as the velocity direction of the incoming solar wind ions. Therefore, the wave polarization in the plasma rest frame remains to be the same with that in the spacecraft frame, which is right handed. The wave properties (plasma rest frame propagation direction and polarization) are thus consistent with that due to the nonresonant ion beam instability. Another wave property to note is that the density roughly has a positive correlation with the magnetic field (Figure 2a) and is increased in the irregular waveforms by about a factor of ~2, compared to that in the linear wave interval.

The nonresonant instability identification is further supported by the ion distributions. Figure 4a shows an ion distribution taken from the linear wave interval. The color represents the averaged phase space density for the energy range of 50–4,000 eV, as a function of the instrument polar (θ) and azimuthal angles (φ). The intense solar wind population is concentrated at $-45° < \theta < 45°$ and $140° < \varphi < 220°$ bounded by the black dashed lines, separated from the backstreaming beam (likely to be shock reflected ions). We calculate the partial moments for the above-mentioned energy and angular range to represent those for solar wind ions and the moments in the complementary energy and angular range for the beam. Figure 4b shows the reduced ion distribution in the $v_x - v_z$ plane at the same time in the spacecraft frame, which shows the two ion populations mostly counterstreaming along the background magnetic field, where the white and magenta diamonds mark their individual bulk velocities. Both ion populations have a common drift velocity of ~−200 km/s along v_y (not shown). Based on the obtained wave propagation properties in the linear wave interval based on the magnetic field correlation analysis, we calculate the cyclotron resonant velocity ($\boldsymbol{V_{res}}$) using Equation 1. The resulting spacecraft frame $\boldsymbol{V_{res}}$ is $-257\ \hat{\boldsymbol{x}}$ km/s with $n = 1$ and $-491\ \hat{\boldsymbol{x}}$ km/s with

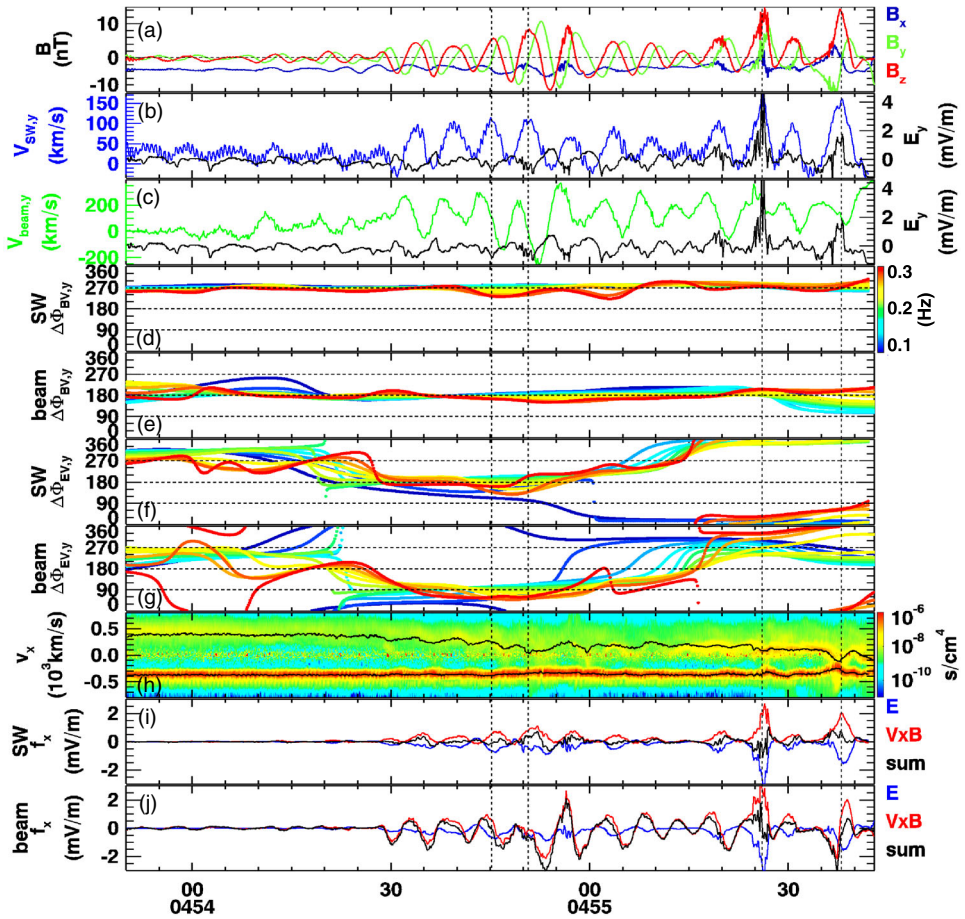

Figure 5. Interaction between ions and the wave fields. (a) Magnetic field. (b) The *y* component of the solar wind velocity (blue) and the electric field (black). (c) The *y* component of the beam (green) and the electric field (black). The vertical dashed lines mark example locations where the solar wind V_y reaches the maximum, and the phase of other variables could be compared with. (d)–(g) The wavelet phase difference of the *y* components between $\boldsymbol{B}$ and $\boldsymbol{V_{SW}}$, between $\boldsymbol{B}$ and $\boldsymbol{V_{beam}}$, between $\boldsymbol{E}$ and $\boldsymbol{V_{SW}}$, and between $\boldsymbol{E}$ and $\boldsymbol{V_{beam}}$. (h) Reduced ion spectrogram along v_x, showing the variations of the velocities for the SW (most intense around $v_x \sim -400$ km/s) and beam (with $v_x > 0$) ions. The overplotted black curves mark the calculated bulk velocities of the two populations. (i, j) The terms in the *x* component of the momentum equation for solar wind and beam ions, respectively, including E (blue), $V \times B$ (red), and the sum of the two (black). Quantities in (b)–(g) and (i) and (j) are in the field-aligned coordinate in the plasma rest frame determined by the bulk ion velocity in the quasi-linear wave interval. The spectrogram in (h) is in the spacecraft frame.

$n = -1$, far from the beam component ($V_{beam,x} = 393$ km/s), consistent with the nonresonant mode where beam ions are not in resonance. Compared to the beam ions, $\boldsymbol{V_{res}}$ is closer to the solar wind population ($V_{SW,x} = -375$ km/s) (~3.3 $V_{SW,th}$ away for both $n = 1$ and $n = -1$ solutions), where $V_{SW,th} = 30$ km/s is the solar wind thermal speed based on a temperature of 5 eV from OMNI data set, though the solar wind ions do not rigorously satisfy the resonant condition of $|V_{res}\text{-}V_0| < V_{th}$. In theory, the exact resonant condition could be achieved by the solar wind ions in many cases of the nonresonant mode wave (Akimoto et al., 1993; Weidl et al., 2019).

We further examine the instability condition with the dispersion relation based on distributions. The velocity space boundary shown in Figure 4a is valid for separating the two ion populations until 04:55:43 UT, allowing us to determine their partial moments. The average moments during 04:53:50–04:54:00 UT are taken to represent the initial conditions for the two populations. The total number density based on electron measurements is $n_0 = 5.5$ cm^{-3}, n_{beam}/n_0 is 0.08, the relative drift is 765 km/s = 23.2 V_A along $\boldsymbol{B_0}$, and 171 km/s = 5.2 V_A perpendicular to $\boldsymbol{B_0}$. The calculated total temperature from the partial moments for solar wind ions is 20 eV. Considering that the instrument may not resolve

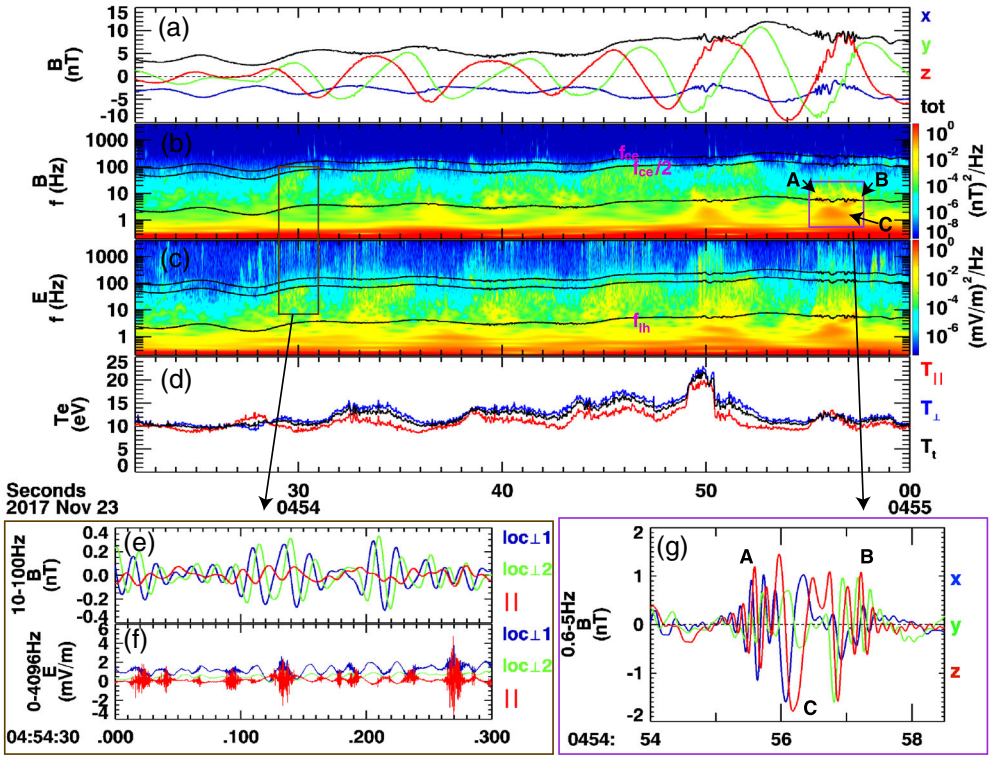

Figure 6. Secondary waves and electron heating inside the ULF wave. (a) Magnetic field. (b, c) Wavelet wave power spectra for the magnetic fields and electric fields. (d) Electron temperature. (e) Filtered 10- to 100-Hz magnetic field waveform for a near $f_{ce}/2$ whistler wave packet marked by the brown box in top panels. (f) Electric fields showing $E_{||}$ bursts with a modulation frequency close to the whistler wave frequency. The parallel direction in (e) and (f) is defined by the 128 samples/s magnetic field data. (g) Magnetosonic whistler wave magnetic field waveform at 0.6–5 Hz during the time marked by the purple box in top panels.

the narrow distributions of solar wind ions, we take the ion temperature from OMNI data set of 5 eV to represent solar wind ion temperature (T_{sw}), so the corresponding β_{sw} relative to $|B_0| = 3.5$ nT is 0.8. The beam total temperature is calculated to be $T_{\text{beam}} = 901$ eV (180 T_{sw}), with $\frac{T_{beam\perp}}{T_{beam||}} = 1.5$, where $T_{beam||} = T_{beam,xx}$ and $T_{beam\perp} = (T_{beam,yy}+T_{beam,zz})/2$. The beam distribution along v_y is colder than that along v_z (not shown), so that the obtained $T_{beam\perp}/T_{beam||}$ is smaller than that appears in the distribution in Figure 4b. The nongyrotropy between $T_{beam,yy}$ and $T_{beam,zz}$ is neglected for this study. The electron bulk velocity [−365, −9, 11] km/s is roughly equal to the ion bulk velocity [−387, −32, 14] km/s in GSE in the spacecraft frame, with near-zero net current. The electron temperature is $T_e = 13$ eV, and the corresponding β_e is 2.3.

The linear instability analysis results for ion beam instabilities with two ion and one electron populations are shown in Figures 4c and 4d, where the dispersion solver BO (Xie, 2019) has been used for solving the dispersion relation. The analytical dispersion relation can be found in Equations 1 and 2 in Gary (1991). The above parameters of two ion and one electron populations with the drift-Maxwellian distribution are input to the dispersion solver, except that the perpendicular drift is set to zero (the effect of the perpendicular drift will be discussed later). The velocities are transformed to the plasma rest frame. The dispersion relation at $k_x > 0$ is for waves propagating toward the beam direction, representing the right-hand resonant mode; the dispersion relation at $k_x < 0$ is for waves propagating in the solar wind ions direction, representing the nonresonant mode. $k_\perp$ is set to zero for the dispersion curves in Figures 4c and 4d, while we have confirmed that the field-aligned propagation gives the maximum growth rate. The resonant mode is unstable with a maximum growth rate of $0.24\omega_{ci}$ at $|kd_i| = 0.07$. The nonresonant mode has larger growth rates than the resonant mode, consistent with the observation that waves of the nonresonant mode dominate. The maximum growth rate is $0.64\omega_{ci}$ at $|kd_i| = 0.64$, while the growth rate curve is relatively flat in a wide k range. The blue dot marks the

real frequency and wavenumber deduced from the magnetic field correlation analysis for the quasi-linear wave interval, which lies in the k range with positive growth rates and is close to the dispersion curve (blue curve in Figure 4c). Adding a perpendicular drift between the two ion populations as in observations only has a minor effect of the instability, reducing the wavenumber of the maximum growth rate for the nonresonant mode from $kd_i = 0.64$ to $kd_i = 0.61$, and the maximum growth rate also occurs at field-aligned propagation We also note that during the interval shown in Figure 2, n_b/n_0 changes from 0.08 to 0.4, $V_{d||}/V_A$ changes from 23 to 15, and T_b/T_{sw} varies between 100 and 300. The instability analyses for such a range of parameters all predict the right-hand nonresonant mode as the dominant instability.

3.2. Wave-Ion Interaction

The interaction between the waves and ions is resolved, providing us information about the ion dynamics and energy exchange between waves and ions. The field-aligned electromagnetic instability could lead to phase bunching of plasmas, which can be described by the dispersion relation (e.g., Gary et al., 1986) and the momentum equation (e.g., Wang & Lin, 2003). We repeat the derivation of the phase relation between the wave magnetic field and solar wind/beam ion transverse velocities in the same way as in Wang and Lin (2003), since the reversal of the B_0 direction compared to Wang and Lin (2003) case changes the phase relation. According to the observations, let us neglect the perpendicular relative drift between the ions and neglect the $\mathbf{k}$ component perpendicular to $\boldsymbol{B_0}$. Solar wind ions drift with $V_{0,SW} < 0$ (along $-x$) and beam ions drift with $V_{0,beam} > 0$ (along $+x$); the wavenumber is $\mathbf{k} = k_x\,\hat{x}$, where $k_x < 0$. Since the wave is right handed, $B_z = -iB_y$ given $k_x < 0$. For either ion population with an initial drift of V_0, in the cold plasma limit, the momentum equation is

$$m\frac{\mathrm{d}\boldsymbol{V}}{\mathrm{d}t} = e(\boldsymbol{E} + \boldsymbol{V}\times\boldsymbol{B}) \tag{2}$$

$$\rightarrow \frac{\partial \boldsymbol{V}}{\partial t} + \boldsymbol{V}\cdot\nabla\boldsymbol{V} = \alpha(\boldsymbol{E} + \boldsymbol{V}\times\boldsymbol{B}),\ \text{where}\ \alpha = e/m \tag{3}$$

With $\partial/\partial t = -i\omega$, $\nabla = ik_x$ and keeping the first-order terms (with the subscript "1") in the equation gives

$$\begin{aligned} -i(\omega - k_x V_0)V_{1y} &= \alpha E_{1y} - \alpha V_{1z}B_0 - \alpha V_0 B_{1z} \\ -i(\omega - k_x V_0)V_{1z} &= \alpha E_{1z} + \alpha V_{1y}B_0 + \alpha V_0 B_{1y} \end{aligned} \tag{4}$$

The goal is to obtain the relationship between B_{1y} and V_{1y}, so we need to eliminate other variables of E_{1y}, E_{1z}, B_{1z}, and V_{1z}. Applying $\boldsymbol{k}\times\boldsymbol{E} = \omega\boldsymbol{B}$ to eliminate the electric field, using the polarization condition of $B_z = -iB_y$ to eliminate B_{1z}, and combining the two components of the equations to eliminate V_{1z}, we get

$$\frac{\alpha B_{1y}}{V_{1y}} = k_x \frac{\frac{\omega}{k_x} - V_0 + \frac{\Omega_{ci}}{kx}}{\frac{\omega}{k_x} - V_0} \tag{5}$$

where $\Omega_{ci} = eB_0/m_i$ and $\omega = \omega_r + i\gamma$. Therefore, the right-hand side of Equation 5 is a complex number and provides the phase relation between V_{1y} and B_{1y}. For beam ions, because they are not resonant with the wave, $V_{0,\,beam} \gg \left|\frac{\omega_r}{k_x}\right|, \left|\frac{\gamma}{k_x}\right|$, and $\left|\frac{\Omega_{ci}}{k_x}\right|$, so that the right-hand side of Equation 5 is ~k_x (a real negative number) ➔ the phase difference between V_{1y} and B_{1y} is close to 180°. $V_{0,SW}$ is close to the other two terms in the numerator ($\left|\frac{\omega_r}{k_x}\right|$ and $\left|\frac{\Omega_{ci}}{k_x}\right|$), so that the real and imaginary parts of Equation 5 are comparable. Taking the observed values of $V_{0,sw} = -1.86\ V_A$, $V_{0,\mathrm{beam}} = 21.34\ V_A$, $V_{ph} = \frac{\omega_r}{\mathrm{k_x}} = -1.4\ V_A$, $\frac{\omega_r}{\Omega_{ci}} = 0.28$, and $kd_i = 0.26$ and using the growth rate of the linear instability analysis for the nonresonant mode at $kd_i = 0.26$ ($\frac{\gamma}{\Omega_{ci}} = 0.52$), the phase difference between B_{1y} and V_{1y} is $\Delta\Phi_{BV,SW} = 290°$ for solar wind ions and $\Delta\Phi_{BV,beam} = 181°$ for beam ions.

The observed phase relationship between **B** and **V** agrees with the above theoretical expectation. Figure 5a shows the magnetic field, and Figures 5b (blue curve) and 5c (green curve) show $V_{SW,y}$ and $V_{beam,y}$,

respectively. Four vertical dashed lines mark locations where $V_{SW,y}$ reaches the maximum, while at the same time, B_y is close to zero during the rise, and $V_{beam,y}$ is in the middle phase of the decrease. The phase relationship is further quantified by the wavelet correlation analysis, which calculates the phase difference between the wavelet transformation of B_y versus $V_{SW,y}$ (Figure 5d) and B_y versus $V_{beam,y}$ (Figure 5e), respectively. Each curve represents one frequency bin, and the blue to red colors represent increasing frequencies between 0.1 and 0.3 Hz. It is clear that $\Delta\Phi_{BV}$ for the solar wind ions is close to 270° and that for beam ions is close to 180°, as expected. As also found in simulations by Wang and Lin (2003), although the theoretical analysis of the B-V phase relationship uses the linear approximation, the relationship remains valid in the nonlinear regime ($|dB|/|B_0| > 1$).

We further investigate the phase relationship between the electric field and ion velocities, which tells us the energy conversion between ions and fields due to the transverse electric field. The black curves in Figures 5b and 5c are E_y, and Figures 5f and 5g show the wavelet phase relationship between E_y and V_y. During the large-amplitude quasi-sinusoidal wave period around 04:54:30–04:55:00 UT, the near-resonant solar wind ions have $\Delta\Phi_{EV}$ between 90° and 180°, so that $\boldsymbol{E}_\perp \cdot \boldsymbol{V}_\perp < 0$ and solar wind ions could lose energies to the wave growth (Gary et al., 1986). During the same interval, $\Delta\Phi_{EV}$ for the beam is slightly smaller than 90°, so beam ions may gain energy from the wave electric fields. At the irregular waveform interval after 04:55:20 UT, $\Delta\Phi_{EV}$ changes to be near zero for solar wind ions and near 270° for the beam, indicating energy gain of the solar wind ions from $\boldsymbol{E}_\perp$ during this phase. Meanwhile, $\Delta\Phi_{EV}$ for beam ions is between 180° and 360°, indicating energy loss of beam ions to $E_\perp$.

In addition to oscillations of the transverse velocities, the velocities along $\boldsymbol{B_0}$ for both ion components decrease. Figure 5h shows the ion spectrogram along x in the spacecraft frame, and the black curves show the obtained velocities for the two ion populations. The beam ions are scattered to occupy a wider velocity space as the wave develops, while the obtained velocities are valid to represent the bulk of the distribution with intense phase-space densities. The variation of the field-aligned velocity is already significant for the beam during the large-amplitude sinusoidal wave interval, where part of the beam ions could have more negative v_x than the solar wind ions, such as around 04:54:51 UT; solar wind ions exhibit slight deceleration during the large-amplitude sinusoidal wave interval, while more significant deceleration occurs in the irregular waveform interval. The x component of the momentum equation 2 for solar wind and beam ions is analyzed in Figures 5i and 5j, which show the force per charge of the E and $V \times B$ terms and the sum of the two. E_x is taken from the x component of $-V_e \times B$, since electrons are mostly frozen-in at the ULF wave scale, while the uncertainty of the E_x measurement is large (up to ~3 mV/m) with spurious spikes for this interval. The analysis is performed in the initial plasma rest frame. For solar wind ions, $V \times B$ is positive, consistent with the ~270° $\Delta\Phi_{BV}$, while it is mostly canceled by the negative E_x. The negative E_x that is mostly balanced by $V \times B$ was previously suggested by the MHD theory and simulation (Zirakashvili & Ptuskin, 2008) and the particle-in-cell simulation (Kobzar et al., 2017), while the kinetic physics related to the generation of E_x will require further understanding. Figure 5i shows that the net force tends to be positive, so that solar wind ions could be decelerated along v_x. Since v_x is negative, the negative E_x does positive work for solar wind ions during the sinusoidal wave interval; in the irregular waveform interval, the bulk v_x of solar wind ions in the spacecraft frame is already larger than that of the initial plasma bulk velocity of −320 km/s, so that the negative E_x does negative work in the initial plasma rest frame. In contrast to E_x, the transverse electric fields do negative work in the sinusoidal wave interval and positive work later, as shown in the E-V phase relationship. For beam ions, the $V \times B$ force dominates over E. Although $\Delta\Phi_{BV}$~180°, a DC drift perpendicular to the x direction exists, which contributes to the oscillating $V \times B$ and is associated with the periodic v_x variations (Figure 5h).

3.3 Secondary Waves Inside the ULF Wave

The ULF wave leads to electron heating and secondary waves. Figure 6 shows that whistler waves with the wavelet wave power enhancements (Figures 6b and 6c) at $f \sim 45$ Hz slightly below $f_{ce}/2 = 70$ Hz, enhanced electron temperature (T_e), and $T_{e\perp}/T_{e\parallel}$ repeatedly occur at roughly the ULF wave period. These wave packets have right-hand polarization and small wave normal angles (θ_{kB}) of 11~21° determined by the Minimum Variance Analysis (MVA) (not shown), which further support their wave mode to be whistler. The whistler wave is likely generated due to the electron perpendicular anisotropy. Field-aligned electron

beams occasionally exist (not shown) but do not exhibit correlation with the ~$f_{ce}/2$ whistler wave occurrence and hence is less likely to be the source of its free energy. Additional higher-frequency electrostatic $E_{||}$ fluctuations exist in the whistler interval, as seen in the electric field wave power spectrum. Figures 6e and 6f zoom in a whistler interval marked by the brown box in Figures 6b and 6c, showing that the electrostatic bursts are mainly in $E_{||}$ with the modulation frequency of ~43 Hz(13 bursts during 0.3 s) close to the whistler frequency, suggesting that the whistler wave may accelerate electrons and excite higher-frequency waves (An et al., 2019; Li et al., 2018). We note that the electron heating has a similar frequency with the ULF wave; however, the $T_{e\perp}$ maximum is not well collocated with the maximum of the magnetic field strength. It indicates that the magnetic field variation of the ULF wave may play a role in heating electrons such as through the betatron mechanism, but the electron perpendicular heating is not completely adiabatic. In most cases, $T_{e||}$ varies together with $T_{e\perp}$, suggesting the possible role of pitch angle diffusion to lower the level of anisotropy [Summers, 2005; Shi et al., 2020]. The exact electron heating mechanism requires further understanding in future with the assistance of simulations.

Another type of secondary wave is the magnetosonic whistler wave with the spacecraft frame frequency close to the lower-hybrid frequency (f_{lh}), often termed as "1-s wave" (e.g., review by Wilson, 2016). (The plasma rest frame frequency is smaller). The whistler mode is manly based on the right-hand polarization in the plasma rest frame (not shown). An example wave packet is marked by the purple box in Figure 6b, which contains two short packets (A and B) at 3–5 Hz on top of one packet (C) at 0.6–3 Hz. The corresponding magnetic field waveform at 0.6–5 Hz is shown in Figure 5g. With the four-spacecraft correlation analysis and MVA, we determined that packets A and C propagate mainly toward the positive y direction in both the spacecraft and plasma rest frame, while packet B propagates toward the positive x direction (sunward) in the plasma rest frame and antisunward in the spacecraft frame. Using the <0.3-Hz magnetic field as the background field, the wave normal angles of the three wave packets are similarly at 52~59°. The highly oblique propagation is distinct from the near $f_{ce}/2$ whistler wave.

4. Conclusions

We studied an event of 3-s ULF waves using MMS observations at the marginally quasi-parallel portion of the Earth's foreshock region. The main findings are summarized as follows.

1. The plasma rest frame wave properties are obtained from multiple methods to be propagated antisunward with right-handed polarization, consistent with the wave due to the ion/ion nonresonant mode instability. Although the uncertainty of determining the spacecraft frame V_{ph} could be comparable to the difference between V_{ph} and the ion bulk velocity in the spacecraft frame, we could further justify the instability mode by ion distributions. The fact that beam ion velocity is far from the estimated cyclotron resonant velocity and the instability analysis is based on the distribution in the linear wave stage both confirms the ion/ion nonresonant mode instability.
2. The interaction between the wave and ions is resolved. For solar wind ions, during the large-amplitude sinusoidal wave interval, the transverse wave electric fields do negative work (based on the phase relationship), while $E_x < 0$ develops and does positive work. The near-orthogonal transverse V-B phase relation leads to a positive x component of $V \times B$, which slightly wins over the negative E_x and leads to net deceleration of solar wind ions to less negative v_x values. Beam ions are not in resonance with the wave. The phase relationship indicates that beam ions gain energy from the transverse fields, while they experience a deceleration along v_x due to E_x. The roles of the longitudinal and transverse fields on solar wind and beam ions are reversed when the wave fields grow further to irregular waveforms.
3. The ULF wave also leads to periodic electron heating and causes perpendicular electron temperature anisotropy that further excites whistler waves slightly below $f_{ce}/2$ and higher-frequency electrostatic waves. Magnetosonic whistler waves with the spacecraft frame frequency near f_{lh} are also generated as another type of the secondary waves inside ULF waveforms.

In this study, we use the gyrotropic drift-Maxwellian distribution to model the backstreaming beam, while the observed distribution (Figure 4b) is not perfectly Maxwellian. Based on previous studies of ion/ion instability due to non-Maxwellian beam distributions, the gyrotropic ring beam distribution (a gyrotropic ring in the perpendicular plane plus a parallel drift) excites waves that propagate along the magnetic fields with the same properties with the regular resonant/nonresonant modes for gyrotropic Maxwellian beams,

while additional oblique wave modes exist (e.g., Killen et al., 1995). In the present observation, the wave is close to the parallel propagation, and using a gyrotropic drift-Maxwellian distribution is sufficient to explain the main feature of the wave. It requires future work to investigate the effects of non-Maxwellian components of the distribution, such as the ring component and the nongyrotropy. We will also perform statistical studies of the 3-s ULF waves to understand whether their source instability is always the nonresonant mode ion/ion beam instability and whether/how ULF waves could be related to structures like shocklets and short large-amplitude magnetic structures (SLAMS) (e.g., Wilson, 2016).

Data Availability Statement

MMS data are available at MMS Science Data Center (https://lasp.colorado.edu/mms/sdc/public/). OMNI data are from https://cdaweb.gsfc.nasa.gov/index.html/, and ARTEMIS data are from http://themis.ssl.berkeley.edu/ website.

Acknowledgments

S. W. thanks Dr. Lynn B. Wilson III for the helpful discussions. The research is supported in part by DOE Grants DESC0016278 and DESC0020058, NSF Grants AGS-1619584 and AGS-2010231, NASA 80NSSC18K1369, and the NASA MMS mission.

References

Akimoto, K., Winske, D., Gary, S. P., & Thomsen, M. F. (1993). Nonlinear evolution of electromagnetic ion beam instabilities. *Journal of Geophysical Research*, *98*(A2), 1419–1433. https://doi.org/10.1029/92JA02345

An, X., Li, J., Bortnik, J., Decyk, V., Kletzing, C., & Hospodarsky, G. (2019). Unified view of nonlinear wave structures associated with whistler-mode chorus. *Physical Review Letters*, *122*(4), 045101. https://doi.org/10.1103/PhysRevLett.122.045101

Argall, M. R., Fischer, D., Le Contel, O., Mirioni, L., Torbert, R. B., Dors, I., et al. (2018). The Fluxgate-Searchcoil Merged (FSM) magnetic field data product for MMS, ArXiv. https://arxiv.org/abs/1809.07388

Bellan, P. M. (2016). Revised single-spacecraft method for determining wave vector k and resolving space-time ambiguity. *Journal of Geophysical Research: Space Physics*, *121*, 8589–8599. https://doi.org/10.1002/2016JA022827

Blanco-Cano, X., Le, G., & Russel, C. T. (1999). Identification of foreshock waves with 3-s periods. *Journal of Geophysical Research*, *104*(A3), 4643–4656. https://doi.org/10.1029/1998JA900103

Chi, P. J., Russell, C. T., & Le, G. (1994). Pc3 and Pc4 activity during a long period of low interplanetary magnetic field cone angle as detected across the Institute of Geological Sciences Array. *Journal of Geophysical Research*, *99*(A6), 11,127–11,139. https://doi.org/10.1029/94JA00517

Eastwood, J. P., Balogh, A., Lucek, E. A., Mazelle, C., & Dandouras, I. (2003). On the existence of Alfven waves in the terrestrial foreshock. *Annales de Geophysique*, *21*(7), 1457–1465. https://doi.org/10.5194/angeo-21-1457-2003

Eastwood, J. P., Balogh, A., Lucek, E. A., Mazelle, C., & Dandouras, I. (2005). Quasi-monochromatic ULF foreshock waves as observed by the four-spacecraft Cluster mission: 1. Statistical properties. *Journal of Geophysical Research*, *110*, A11219. https://doi.org/10.1029/2004JA010617

Eastwood, J. P., Lucek, E. A., Mazelle, C., Meziane, K., Narita, Y., Pickett, J., & Treumann, R. (2005). The foreshock. *Space Science Reviews*, *118*(1–4), 41–94. https://doi.org/10.1007/s11214-005-3824-3

Engebretson, M. J., Cahill, L. J., Arnoldy, R. L., Anderson, B. J., Rosenberg, T. J., Carpenter, D. L., et al. (1991). The role of the ionosphere in coupling upstream ULF wave power into the dayside magnetosphere. *Journal of Geophysical Research*, *96*(A2), 1527–1542. https://doi.org/10.1029/90JA01767

Ergun, R. E., Tucker, S., Westfall, J., Goodrich, K. A., Malaspina, D. M., Summers, D., et al. (2016). The axial double probe and fields signal processing for the MMS mission. *Space Science Reviews*, *199*(1–4), 167–188. https://doi.org/10.1007/s11214-014-0115-x

Farris, M. H., Petrinec, S. M., & Russell, C. T. (1991). The thickness of the magnetosheath: Constraints on the polytropic index. *Geophysical Research Letters*, *18*(10), 1821–1824. https://doi.org/10.1029/91GL02090

Gary, S. P. (1991). Electromagnetic ion/ion instabilities and their consequences in space plasmas: A review. *Space Science Reviews*, *56*(3–4), 373–415. https://doi.org/10.1007/BF00196632

Gary, S. P., Thomsen, M. F., & Fuselier, S. A. (1986). Electromagnetic instabilities and gyrophase-bunched particles. *The Physics of Fluids*, *29*, 531. https://doi.org/10.1063/1.865441

Gershman, D., Viñas, A., Dorelli, J. C., Goldstein, M. L., Shuster, J., Avanov, L. A., et al. (2018). Energy partitioning constraints at kinetic scales in low-β turbulence. *Physics of Plasmas*, *25*, 022303. https://doi.org/10.1063/1.5009158

Hobara, Y., Walker, S. N., Balikhin, M., Pokhotelov, O. A., Dunlop, M., Nilsson, H., & Rème, H. (2007). Characteristics of terrestrial foreshock ULF waves: Cluster observations. *Journal of Geophysical Research*, *112*, A07202. https://doi.org/10.1029/2006JA012142

Killen, K., Omidi, N., Krauss-Varban, D., & Karimabadi, H. (1995). Linear and nonlinear properties of ULF waves driven by ring-beam distribution functions. *Journal of Geophysical Research*, *100*(A4), 5835–5852. https://doi.org/10.1029/94JA02899

Kobzar, O., Niemiec, J., Pohl, M., & Bohdan, A. (2017). Spatio-temporal evolution of the non-resonant instability in shock precursors of young supernova remnants. *Monthly Notices of the Royal Astronomical Society*, *469*, 4985–4998. https://doi.org/10.1093/mnras/stx1201

Le Contel, O., Leroy, P., Roux, A., Coillot, C., Alison, D., Bouabdellah, A., et al. (2016). The search-coil magnetometer for MMS. *Space Science Reviews*, *199*, 257–282. https://doi.org/10.1007/s11214-014-0096-9

Le, G., Russell, C. T., Thomsen, M. F., & Gosling, J. T. (1992). Observations of a new class of upstream waves with periods near 3 seconds. *Journal of Geophysical Research*, *97*(A3), 2917–2925. https://doi.org/10.1029/91JA02707

Li, H., Pang, Y., Huang, S., Zhou, M., Deng, X., Yuan, Z., et al. (2013). The turbulence evolution in the high β region of the Earth's foreshock. *Journal of Geophysical Research: Space Physics*, *118*, 7151–7159. https://doi.org/10.1002/2013JA019424

Li, J., Bortnik, J., An, X., Li, W., Russell, C. T., Zhou, M., et al. (2018). Local excitation of whistler mode waves and associated Langmuir waves at dayside reconnection regions. *Geophysical Research Letters*, *45*, 8793–8802. https://doi.org/10.1029/2018GL078287

Lindqvist, P.-A., Olsson, G., Torbert, R. B., King, B., Granoff, M., Rau, D., et al. (2016). The spin-plane double probe electric field instrument for MMS. *Space Science Reviews*, *199*(1–4), 137–165. https://doi.org/10.1007/s11214-014-0116-9

Mazelle, C., Meziane, K., LeQuéau, D., Wilber, M., Eastwood, J. P., Rème, H., et al. (2003). Production of gyrating ions from nonlinear waveparticle interaction upstream from the Earth's bow shock: A case study from Cluster-CIS. *Planetary and Space Science*, *51*(12), 785–795. https://doi.org/10.1016/j.pss.2003.05.002

Pinc̦on, J. L., & Motschmann, U. (1998). Multi-spacecraft filtering: General framework. In G. Paschmann & P. W. Daly (Eds.), *Analysis Methods for Multi-Spacecraft Data* (pp. 65–78). Bern, Switzerland: Int. Space Sci. Inst.

Pollock, C., Moore, T., Jacques, A., Burch, J., Gliese, U., Saito, Y., et al. (2016). Fast plasma investigation for magnetospheric multiscale. *Space Science Reviews*, *199*, 331–406. https://doi.org/10.1007/s11214-016-0245-4

Robert, P., Dunlop, M. W., Roux, A., & Chanteur, G. (1998). Accuracy of current density determination. *ISSI Scientific Reports Series*, *1*, 395–418.

Russell, C. T., Anderson, B. J., Baumjohann, W., Bromund, K. R., Dearborn, D., Fischer, D., et al. (2016). The magnetospheric multiscale magnetometers. *Space Science Reviews*, *199*, 189–256. https://doi.org/10.1007/s11214-014-0057-3

Schwartz, S. J. (1998). Analysis methods for multi-spacecraft data. ISSI Scientific Reports Series, 1, 249.

Shi, X., Liu, T. Z., Angelopoulos, V., & Zhang, X. -J. (2020). Whistler mode waves in the compressional boundary of foreshock transients. *Journal of Geophysical Research: Space Physics*, *125*, e2019JA027758. https://doi.org/10.1029/2019JA027758

Summers, D. (2005). Quasi-linear diffusion coefficients for field-aligned electromagnetic waves with applications to the magnetosphere. *Journal of Geophysical Research*, *110*, A08213. https://doi.org/10.1029/2005JA011159

Wang, B., Nishimura, Y., Zhang, H., Shen, X.-C., Lyons, L., Angelopoulos, V., et al. (2019). The 2-D structure of foreshock-driven field line resonances observed by THEMIS satellite and ground-based imager conjunctions. *Journal of Geophysical Research: Space Physics*, *124*, 6792–6811. https://doi.org/10.1029/2019JA026668

Wang, X. Y., & Lin, Y. (2003). Generation of nonlinear Alfven and magnetosonic waves by beam-plasma interaction. *Physics of Plasmas*, *10*(9), 3528. https://doi.org/10.1063/1.1599359

Weidl, M. S., Winske, D., & Niemann, C. (2019). On the background-gyroresonant character of Bell's instability in the large-current regime. *The Astrophysical Journal*, *872*, 48. https://doi.org/10.3847/1538-4357/aafad0

Wilson, L. B. III (2016). Low frequency waves at and upstream of collisionless shocks. In A. Keiling, D.-H. Lee, & V. Nakariakov (Eds.), *Low-frequency Waves in Space Plasmas*, *Geophysical Monograph Series* (Vol. 216, pp. 269–291). Washington, D. C: AGU. https://doi.org/10.1002/9781119055006.ch16

Winske, D., & Leroy, M. M. (1984). Diffuse ions produced by electromagnetic ion beam instabilities. *Journal of Geophysical Research*, *89*(A5), 2673–2688. https://doi.org/10.1029/JA089iA05p02673

Xie, H. (2019). BO: A unified tool for plasma waves and instabilities analysis. *Computer Physics Communications*, *244*, 343–371. https://doi.org/10.17632/cvbrftzfy5.1

Yeoman, T. K., Wright, D. M., Engebretson, M. J., Lessard, M. R., Pilipenko, V. A., & Kim, H. (2012). Upstream generated Pc3 ULF wave signatures observed near the Earth's cusp. *Journal of Geophysical Research*, *117*, A03202. https://doi.org/10.1029/2011JA017327

Zirakashvili, V. N., & Ptuskin, V. S. (2008). Modeling Bell's nonresonant cosmic-ray instability. *The Astrophysical Journal*, *678*, 255–261. https://doi.org/10.1086/529579